



Substituent effects of Ba^{2+} for Sm^{3+} on the structure and electrochemical performances of $\text{Sm}_{0.5}\text{Sr}_{0.5}\text{Co}_{0.8}\text{Fe}_{0.2}\text{O}_{3-\delta}$ cathode for intermediate temperature solid oxide fuel cells

Jianquan Gao ^a, Xiwen Song ^{b,*}, Fen Zhou ^b, Shengli An ^{b,*}, Yanwen Tian ^a

^aMaterial and Metallurgy College, Northeastern University, Shenyang 114001, China

^bSchool of Materials and Metallurgy, Inner Mongolia University of Science and Technology, Baotou 014010, China

HIGHLIGHTS

- A novel series of perovskite-type cathode materials $\text{Sm}_{1-x}\text{Ba}_x\text{Sr}_{0.5}\text{Co}_{0.8}\text{Fe}_{0.2}\text{O}_{3-\delta}$ ($0 \leq x \leq 0.2$) for solid state oxide fuel cells are prepared by a citric-nitrate process.
- Among the series of the samples, the highest conductivity was observed for $\text{Sm}_{0.45}\text{Ba}_{0.05}\text{Sr}_{0.5}\text{Co}_{0.8}\text{Fe}_{0.2}\text{O}_{3-\delta}$ to be 1250 Scm^{-1} in air at 300°C .
- The partial substitution of Ba for Sm site obviously enhanced the cathode materials.
- The cathode with the composition $x = 0.2$ exhibits the lowest area specific resistance, which is $0.032 \Omega\text{cm}^2$ at 750°C and $0.056 \Omega\text{cm}^2$ at 700°C .
- The cell with the composition $x = 0.20$ gives the maximum power density of 1030 mW cm^{-2} at 650°C .

ARTICLE INFO

Article history:

Received 19 March 2012

Received in revised form

23 May 2012

Accepted 24 May 2012

Available online 3 July 2012

Keywords:

Intermediate temperature operating solid oxide fuel cell

Cathode

Perovskites

ABSTRACT

Perovskite oxides $\text{Sm}_{1-x}\text{Ba}_x\text{Sr}_{0.5}\text{Co}_{0.8}\text{Fe}_{0.2}\text{O}_{3-\delta}$ ($x = 0, 0.05, 0.10, 0.15, 0.20$) have been synthesized by a citric acid method. The X-ray diffractometer results show that all samples exhibit a perovskite structure with orthorhombic symmetry. The X-ray diffractometer, Infrared spectroscopy and Raman spectroscopy results suggest an increase in the cell volume with Ba content. The X-ray Photoelectron spectra result suggests that the valence change of partial Co from $3+$ to $4+$ and the formation of oxygen vacancy are two mechanisms to satisfy charge neutrality when Sm^{3+} is partially substituted by Ba^{2+} . The cathode polarization measurement of the symmetric cells with SBSCF cathodes shows that the area specific resistance decreases with the increase of Ba^{2+} substitution. The cathode with the composition $x = 0.2$ exhibits the lowest area specific resistance, which is $0.032 \Omega\text{cm}^2$ at 750°C and $0.056 \Omega\text{cm}^2$ at 700°C . The performance of $\text{Sm}_{0.2}\text{Ce}_{0.8}\text{O}_{2-\delta}/\text{Ni}$ anode-supported cells using $\text{Sm}_{1-x}\text{Ba}_x\text{Sr}_{0.5}\text{Co}_{0.8}\text{Fe}_{0.2}\text{O}_{3-\delta}$ as cathode exhibits that the power density increase with increasing Ba^{2+} content. The cell with the composition $x = 0.20$ gives the maximum power density of 1030 mW cm^{-2} at 650°C and 285 mW cm^{-2} at 500°C . These results suggest that Ba^{2+} substituent substantially improves the electrochemical performance of $\text{Sm}_{0.5}\text{Sr}_{0.5}\text{Co}_{0.8}\text{Fe}_{0.2}\text{O}_{3-\delta}$, makes it a promising cathode material for intermediate temperature solid oxide fuel cells.

© 2012 Elsevier B.V. All rights reserved.

1. Introduction

Development of novel oxides with high mixed ionic and electronic conductivity (MIEC) is of great significance to improve the performance of the electrochemical devices, which include solid oxide fuel cells [1–4], oxygen separation process [5,6] and catalyst [7,8]. In the case of solid oxide fuel cells, in order to decrease the substantial polarization resistance increase associated with the

reduction of the operation temperature to the intermediate range (500 – 800°C), mixed conducting oxides with perovskite and perovskite-related intergrowth structure such as $\text{Ln}_{1-x}\text{Sr}_x\text{MO}_3$ ($\text{M} = \text{Mn, Fe, Ni and Co}$) [9–12], $\text{Ln}_2\text{NiO}_{4+\delta}$ [13–15] and $\text{LnBaCo}_2\text{O}_{5+\delta}$ [16–19] have been widely investigated as cathode candidates. The mixed conductivity of such materials greatly extends the reaction active sites, and consequently, these materials are expected to provide much higher electrode activity for oxygen reduction than $\text{La}_{1-x}\text{Sr}_x\text{MnO}_3$ at reduced temperatures.

Among these mixed conducting oxides, cobalt-based perovskite-type oxides exhibit excellent electrochemical properties, especially in combination with doped-ceria electrolytes. The

* Corresponding authors. Tel.: +86 472 6896122; fax: +86 472 5951572.

E-mail addresses: xiwensong@126.com, songxiwen@imust.cn (X. Song), shengli-an@126.com, san@imust.cn (S. An).

cobalt-containing cathodes studied the most in literature seem to be composition of $\text{Sm}_{0.5}\text{Sr}_{0.5}\text{CoO}_{3-\delta}$ or $\text{La}_{0.6}\text{Sr}_{0.4}\text{Fe}_{0.8}\text{Co}_{0.2}\text{O}_{3-\delta}$ with a ceria-based electrolyte [20–22]. The area specific resistance (ASR) value of a $\text{Sm}_{0.5}\text{Sr}_{0.5}\text{CoO}_{3-\delta}$ composition cathode measured at 600 °C was 0.18 Ωcm² [20]. However, the thermal expansion coefficient of $\text{Sm}_{0.5}\text{Sr}_{0.5}\text{CoO}_{3-\delta}$ is very high as it is a pure cobaltite perovskite, which may make the practical application of this material difficult. The porous $\text{Sm}_{0.5}\text{Sr}_{0.5}\text{CoO}_{3-\delta}$ cathode in contact with $\text{Ce}_{0.8}\text{Sm}_{0.2}\text{O}_{2-\delta}$ electrolyte was reported to undergo fast degradation both on thermal cycling and during isothermal operation [23]. Partial substitution of cerium for cobalt in $\text{Sm}_{1-x}\text{Sr}_x\text{CoO}_{3-\delta}$ was shown to slightly suppress the lattice expansion, to decrease total conductivity, and to improve cathode performance. However, the cerium solubility limit is low, <5 mol% [24]. Crystal structure, thermal expansion coefficient, electrical conductivity, and cathode polarization of $\text{Sm}_{0.5}\text{Sr}_{0.5}\text{Co}_{1-x}\text{Fe}_x\text{O}_{3-\delta}$ (SSCF) ($0 \leq x \leq 0.9$) series have also been studied. However, this substitution leads to an increase in the ASR of SSCF [25]. Alternatively, $\text{Ba}_{0.5}\text{Sr}_{0.5}\text{Co}_{0.8}\text{Fe}_{0.2}\text{O}_{3-\delta}$ (BSCF) exhibits excellent electrochemical performance at low temperatures, thus it has become a very promising cathode material for IT-SOFCs [26]. Furthermore, the electrochemical performance of BSCF can be improved by doping a rare earth element into A sites [27–29]. However, the wide applications of BSCF may be inhibited by three major problems: large coefficient of thermal expansion (CTE) of the BSCF, the collapsing of the desired cubic structure of BSCF at temperatures below 1123 K under long-term condition, and the detriment of the surface oxygen exchange coefficient ascribed to the occurrence of some surface carbonation in the presence of CO_2 .

The intrinsic properties of cathode materials depend on the material composition and lattice structure. One of the intriguing features of ABO_3 perovskite oxide is that their physicochemical properties can be tailored by partial substitution on A and/or B sites with only minimal changes in structure. The improvement in the properties is commonly resulted from the B-site cation modification, due to B-site cation associating to the redox catalytic mechanism. Alternatively, the physicochemical properties can be also tuned by the A-site cation adjustment [30]. For example, A-site substituent with the larger cation Ba^{2+} results in the expansion in the cell volume and the reduction in the binding energy of the crystal [31], which facilitates the oxygen diffusion within the lattice and promotes the oxygen exchange kinetics on the surface of the oxide, consequently leads to an improvement in the cathode performance. However, the investigation of the influence and the mechanism of Ba^{2+} substitution on the properties of the cobalt-containing cathodes are still less understood.

Our work gives a detailed investigation of the effect of Ba^{2+} substitution for Sm^{3+} on the structure and electrochemical performances of $\text{Sm}_{0.5}\text{Sr}_{0.5}\text{Co}_{0.8}\text{Fe}_{0.2}\text{O}_3$ based cathode of intermediate temperature solid oxide fuel cells (IT-SOFCs). $\text{Sm}_{0.5-x}\text{Ba}_x\text{Sr}_{0.5}\text{Co}_{0.8}\text{Fe}_{0.2}\text{O}_{3-\delta}$ ($x = 0 \sim 0.2$) were synthesized using sol–gel method, the structure, electrical conductivity and electrochemical performances were systematically investigated. The compositions with Ba substitution demonstrate decreasing ASR of cathode and increasing power density of the single cell. It should be an intriguing approach to improve the performances of IT-SOFCs.

2. Experimental

2.1. Sample synthesis and cell fabrication

$\text{Sm}_{0.5-x}\text{Ba}_x\text{Sr}_{0.5}\text{Co}_{0.8}\text{Fe}_{0.2}\text{O}_{3-\delta}$ ($x = 0, 0.05, 0.10, 0.15$ and 0.20) powders were synthesized by an EDTA-citrate combined sol–gel process. $\text{Sm}(\text{NO}_3)_3$, $\text{Ba}(\text{NO}_3)_2$, $\text{Sr}(\text{NO}_3)_2$, $\text{Fe}(\text{NO}_3)_2 \cdot 9\text{H}_2\text{O}$ and $\text{Co}(\text{N}_3)_2 \cdot 6\text{H}_2\text{O}$ were used as the raw materials. Stoichiometric amounts

of these raw materials were dissolved into distilled water to form a solution. Into which $\text{EDTA-NH}_3 \cdot \text{H}_2\text{O}$ and citric acid were added in sequence at a molar ratio of 1:1:2 for total metal ions: EDTA: citric acid under heating and stirring. A transparent gel was obtained by evaporating the water from the solution. The gel was pre-heated at 250 °C and followed by calcinations at 950–1000 °C for 5 h in air to obtain the final product with the desired lattice structure.

For electrical conductivity measurement, the powders were uniaxially pressed into bars (5 mm × 5 mm × 40 mm) and sintered at 1150 °C for 10 h. Ag wire (0.25 mm in diameter) and Ag paste were used to make the four probes. To fabricate the symmetric cells for cathode polarization investigation, 20 mol% Sm_2O_3 doped CeO_2 (SDC) powders were synthesized using the same method as above mentioned. The SDC powders were pressed into disk-shaped pellets using a stainless steel die under a pressure of 10 Mpa, followed by sintered at 1450 °C for 5 h in air. The resulted dense pellets have a diameter of ~12.0 mm and thickness of ~1.0 mm. To prepare the electrode layers, $\text{Sm}_{0.5-x}\text{Ba}_x\text{Sr}_{0.5}\text{Co}_{0.8}\text{Fe}_{0.2}\text{O}_{3-\delta}$ suspension which was well dispersed in a mixed solution of ethylene glycol, ethanol and isopropyl alcohol was symmetrically deposited onto both surfaces of the electrolytes by spraying, followed by calcinations at 1000 °C for 2 h. Both electrode surfaces of the symmetric cells were painted with a thin layer of silver to act as current collectors.

To fabricate the anode-supported single cells for the measurement of power density, a mixture of NiO_2 and SDC in the weight ratio of 40:60 was uniaxially pressed into pellets to form the anode. Then SDC powders with a proper amount was homogeneously dispersed over one surface of the anode pellets inside the die and pressed again to form dual layer pellets. These green cells were then sintered at 1450 °C for 5 h in air to densify the electrolyte layer. The $\text{Sm}_{0.5-x}\text{Ba}_x\text{Sr}_{0.5}\text{Co}_{0.8}\text{Fe}_{0.2}\text{O}_{3-\delta}$ suspension was then spray deposited over the other surface of the electrolyte, followed by calcinations at 1000 °C for 2 h in air.

2.2. Characterization

The phase of the synthesized powders was characterized by an X-ray diffractometer (XRD, Bruker D8 Advance) equipped with $\text{Cu K}\alpha$ radiation ($\lambda = 0.15418 \text{ nm}$). The Raman spectra of $\text{Sm}_{0.5-x}\text{Ba}_x\text{Sr}_{0.5}\text{Co}_{0.8}\text{Fe}_{0.2}\text{O}_{3-\delta}$ were collected at RT with a micro Raman spectrometer (JY Labram HR 800) in backscattering geometry with liquid nitrogen cooled CCD detector. Raman scattering was excited using an Ar-ion laser at a wavelength of 514.5 nm. A 90× long working distance objective was used to focus the laser beam onto a spot of about 2 μm in diameter. FT-IR spectra were obtained using a Perkin Elmer Paragon 1000/spectrum RX Fourier IR spectrometer. The samples were mixed with KBr in the mass ratio 5.5–7.0 × 10³:1, and then compacted into pellets with a thickness of 0.75–1.0 mm and a diameter of 11.78 mm under a pressure of 0.4 Gpa. X-ray Photoelectron spectra (XPS) were acquired using a VG Escalab 200R spectrometer equipped with a hemispherical electron analyzer and an $\text{Al K}\alpha$ ($h\nu = 1486.6 \text{ eV}$) X-ray source. Peak intensities were estimated by calculating the integral of each peak after smoothing and subtraction of an S-shaped background and fitting of the experimental peak by a least-squares routine using Gaussian and Lorentzian lines. The binding energy (BE) reference was taken as the C 1s peak from carbon contamination of the samples at 284.6 eV.

Electrical conductivity was measured by the four-probe D.C. technique. The electrical conductivity measurements were performed from 300 to 800 °C at intervals of 10 °C in air. The current and the voltage were detected by a Keithley 2420 source meter.

The symmetric cell was loaded into a quartz tube reactor with controllable atmosphere for electrochemical impedance spectra

(EIS) measurement using a Solartron 1260 Frequency Response Analyzer in combination with a Solartron1287 potentiostat. The frequency used for EIS measurements ranged from 10^{-1} – 10^{-2} to 10^5 – 10^6 Hz with signal amplitude of 10 mV. Samples were tested under open circuit voltage (OCV) condition. Microscopic features of the symmetric cells were characterized using a scanning electron microscope (SEM, Phillips, Quanta-400).

An in-lab constructed fuel cell test station was used to evaluate the electrochemical performance of the fabricated cells. The fuel cell was sealed onto a quartz tube using silver paste to form an anode chamber, which was then heated to 650 °C at a rate of 2 °C min⁻¹ and held for 5 h to set the seal. Hydrogen at a flow rate of 20 ml min⁻¹ [STP] was introduced into the anode chamber to begin in situ reduction of anodic NiO₂ to metallic nickel. After about 5 h, the hydrogen flow rate was increased to 80 ml min⁻¹ [STP] and bubbled through water at 25 °C for I–V cell polarization test. During the test, the cathode was exposed to the ambient atmosphere. I–V curves were collected at 50 °C intervals over a temperature range of 500–650 °C using a digital source meter (model 2420, Keithley, Cleveland) with a four-probe configuration.

3. Results and discussion

3.1. Phase composition and crystal structure of SBSCF

The X-ray diffraction patterns of $\text{Sm}_{0.5-x}\text{Ba}_x\text{Sr}_{0.5}\text{Co}_{0.8}\text{Fe}_{0.2}\text{O}_{3-\delta}$ powders are presented in Fig. 1. All the $\text{Sm}_{0.5-x}\text{Ba}_x\text{Sr}_{0.5}\text{Co}_{0.8}\text{Fe}_{0.2}\text{O}_{3-\delta}$ powders show perovskite structure with an orthorhombic symmetry. For the low substitution composition ($x = 0.05$), the reflections shift to the high angle direction compared with the Barium-free composition, indicating a unit cell contraction. With further increasing Ba²⁺ content, the reflections consistently shift to the low angle direction, which suggests a lattice expansion. It can be seen more clearly from the detail of the main reflection shown in Fig. 1(b). In addition, the unit cell parameters of $\text{Sm}_{0.5-x}\text{Ba}_x\text{Sr}_{0.5}\text{Co}_{0.8}\text{Fe}_{0.2}\text{O}_{3-\delta}$ were calculated and listed in Table 1. With increasing Ba²⁺ substitution, the unit cell parameter a consistently increases, whereas the parameters b , c and the cell volume exhibit a change trend of descend firstly then ascend. The substitution of larger Ba²⁺ (1.75 Å) for Sm³⁺ (1.24 Å) [32] will lead to an increase in the average size of the cations in the A-site, which will extend the A–O bonding length and thereby should expand the unit cell. Whereas, the substitution will result in the transition of B-site cations from lower to higher valences, which will contract the B–O

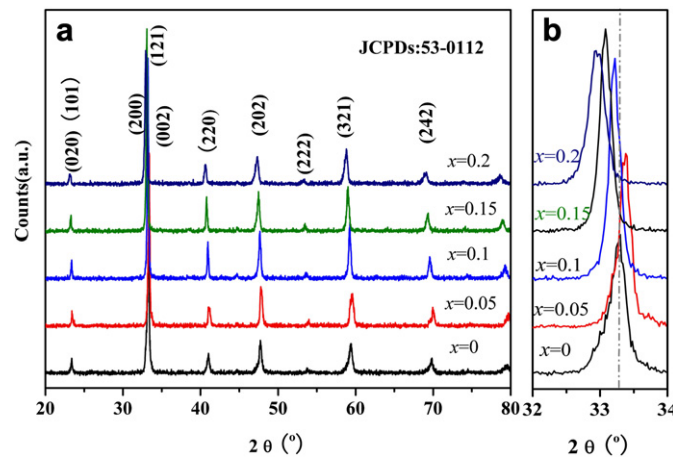


Fig. 1. Powder XRD patterns of the $\text{Sm}_{0.5-x}\text{Ba}_x\text{Sr}_{0.5}\text{Co}_{0.8}\text{Fe}_{0.2}\text{O}_{3-\delta}$ ($0 \leq x \leq 0.2$) samples, 2θ is (a) 20–80°, (b) 32–34°.

Table 1

Cell parameters resulting from the Rietveld Fit of the XRD profiles of the SBSCF samples.

Sample	a (Å)	b (Å)	c (Å)	V (Å ³)
$x = 0$	5.3935	7.6142	5.3838	221.1
$x = 0.05$	5.3989	7.5847	5.3602	219.5
$x = 0.1$	5.4023	7.6122	5.3846	221.44
$x = 0.15$	5.4152	7.6725	5.4218	225.27
$x = 0.2$	5.4358	7.6959	5.4422	227.67

bonding length due to the larger ionic radius of B³⁺ ($r_{\text{Fe}}^{3+} = 0.645$ Å; $r_{\text{Co}}^{3+} = 0.61$ Å) than B⁴⁺ ($r_{\text{Fe}}^{4+} = 0.585$ Å; $r_{\text{Co}}^{4+} = 0.53$ Å) [32]. Therefore, it should lead to a shrinkage in the unit cell. The variation in the unit cell volume is a result of both effects. For the sample with lower Ba²⁺ substitution ($x = 0.05$), the decrease in the unit cell volume demonstrates that the latter show more contribution. For the higher Ba²⁺ content samples, the consistent increase in the unit cell volume with Ba²⁺ content exhibits that the former show more contribution than the latter.

3.2. Raman spectroscopy and Infrared spectroscopy

At room temperature, the structure of $\text{Sm}_{0.5}\text{Sr}_{0.5}\text{Co}_{0.8}\text{Fe}_{0.2}\text{O}_{3-\delta}$ is orthorhombic with space group D_{2h}^{16} – pbm [24]. As shown in Fig. 2, the Co/Fe ions are located at the center of the octahedral environment (in D_{4h} symmetry), the oxygen ions are in apical (in C_{4v} symmetry, denoted as O(1)) and equatorial (in D_{2h} symmetry, denoted as O(2)) positions. Sm and Sr ions are located in a strongly distorted oxygen environment. The Sm, Sr and the oxygen ions constitute a dodecahedral structure, Sm(Sr)O₉. Group theoretical analysis of zone center phonons yield

$$\Gamma = 7\text{A}_g + 7\text{B}_{1g} + 5\text{B}_{2g} + 5\text{B}_{3g} + 8\text{A}_{u} + 8\text{B}_{1u} + 10\text{B}_{2u} + 10\text{B}_{3u} \quad (1)$$

It has four Raman active modes A_g , B_{1g} , B_{2g} , B_{3g} , three infrared active modes B_{1u} , B_{2u} , B_{3u} and one inactive mode A_{u} .

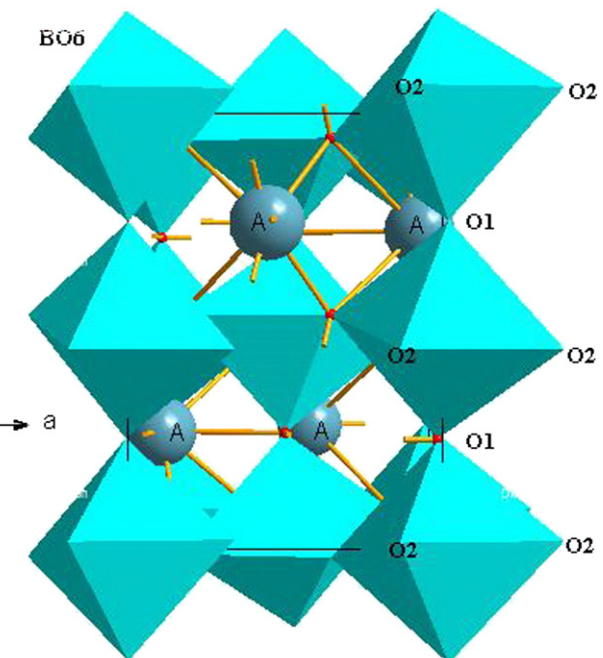


Fig. 2. Schematic picture of the orthorhombic perovskite ABO_3 structure.

Fig. 3 shows the Raman spectra of $\text{Sm}_{0.5-x}\text{Ba}_x\text{Sr}_{0.5}\text{Co}_{0.8}\text{Fe}_{0.2}\text{O}_{3-\delta}$ ($x = 0, 0.05, 0.10, 0.15$ and 0.20) samples in the frequency range of 50 – 800 cm^{-1} . According to group theory mentioned above, one should observe at least 24 Raman-active peaks in orthorhombic D_{2h}^{16} – (pbnm) groups since the peaks corresponding to the same symmetry species cannot overlap. However, the observed number of peaks is less than 24, which should be due to the weaker cross-section of Raman-active modes [33]. Furthermore, several fine distinctions in the bands for the compositions with various Ba^{2+} concentration have been found. The band intensity of the peaks in the particularly low frequency region of ~ 70 – 100 cm^{-1} gradually increases with Ba content. This suggests that they are in relation to vibrations mainly involving Ba and Sr ions, which are the heaviest ions in these compounds and therefore expected to vibrate with the lowest frequency. Whereas, the intensity of the peak at 194 cm^{-1} decreases with increasing Ba^{2+} content until disappears for the composition with $x = 0.2$. This intensity decrease demonstrates a weakening in the deformational motions of the $(\text{Sm}/\text{Ba}/\text{Sr})$ – $[(\text{Co}/\text{Fe})\text{O}_6]$ units, suggesting that the cations and the oxygen have a tendency to occupy their high-symmetry crystallographic sites as Ba^{2+} content increases. The band, peak at around 460 cm^{-1} , corresponding to the vibrations of the A–O(1)–Co oxygen bridge bonds shift from 483 cm^{-1} to 460 cm^{-1} , suggesting an increase in the bond lengths. In addition, as the Ba^{2+} content increases, two new bands at 618 and 645 cm^{-1} appear, which should be attributed to the defect-induced mode or a local distortion of BO_6 octahedron.

BO_6 octahedron, which has A-site cation in their interstitial sites, is the repeatable structure unit of ABO_3 crystalline structure. There are three kinds of vibrations to their IR spectra, and the stretching

vibration (v_3) is IR inactive if three pairs of B–O bonds have the same length, i.e., BO_6 octahedron has high symmetry. On the contrary, the B–O stretching vibration v_3 is IR active if the symmetry of BO_6 is low [34]. As shown in Fig. 4, there are three vibration bands at ~ 450 , 650 and 760 cm^{-1} in the IR spectra of all $\text{Sm}_{0.5-x}\text{Ba}_x\text{Sr}_{0.5}\text{Co}_{0.8}\text{Fe}_{0.2}\text{O}_{3-\delta}$ samples. The vibration band at 450 cm^{-1} , belongs to the bending vibration of Co–O bonding in the BO_6 octahedron, and the bands at 650 and 760 cm^{-1} can be assigned to two kinds of Co–O bond stretching vibration in the BO_6 octahedron [35]. The band at 650 cm^{-1} for the Ba^{2+} containing composition become broad and red shift compared with that for the Barium-free composition, suggesting that some amounts of Co^{3+} change into Co^{4+} when Sm^{3+} are partially replaced by Ba^{2+} . The interaction between Co^{4+} and O is stronger than that of Co^{3+} and O, and thus the wave number of the stretching vibration of Co^{4+} –O is greater than that of Co^{3+} –O. Therefore, the red shift of the wave number of stretching vibration of Co–O bond in the BO_6 octahedron might suggest the formation of some Co^{4+} . For the compositions with $x \geq 0.1$, the stretching mode at 650 cm^{-1} slightly shift towards longer wave numbers with the increase of Ba^{2+} content. This indicates an increase in B–O bond length and consequently an increase in the cell volume. In addition, obvious shoulders on both sides of all bands have been noticed, which should be ascribed to the large lattice distortion associated with larger ionic radius of Ba^{2+} .

3.3. XPS analysis of SBSCF

Fig. 5 shows the XPS spectra of the $\text{Co}2p$ and $\text{O}1s$ level of $\text{Sm}_{0.5-x}\text{Ba}_x\text{Sr}_{0.5}\text{Co}_{0.8}\text{Fe}_{0.2}\text{O}_{3-\delta}$. Fig. 5(a) represents two main peaks

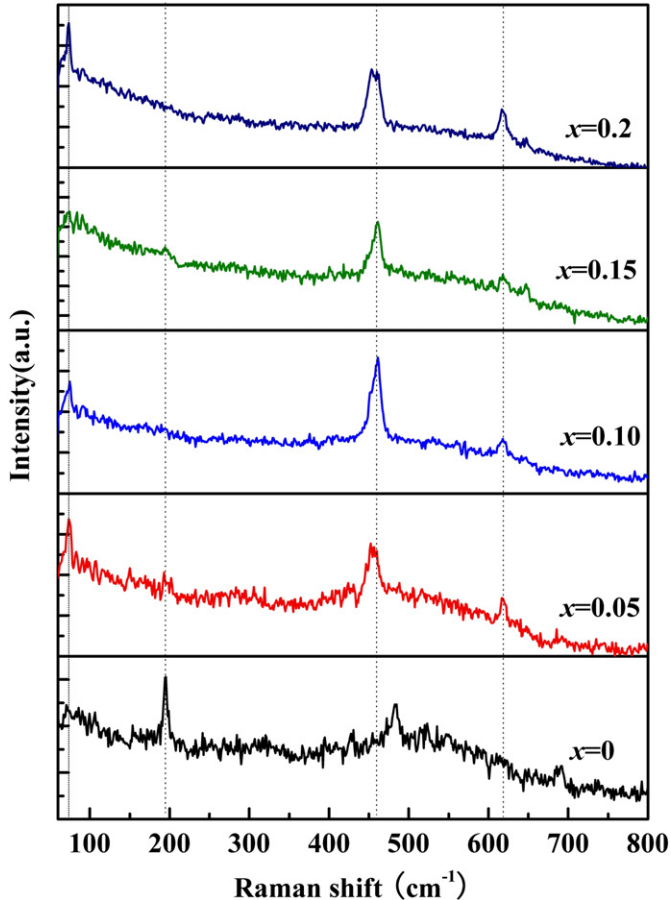


Fig. 3. Raman spectra of the $\text{Sm}_{0.5-x}\text{Ba}_x\text{Sr}_{0.5}\text{Co}_{0.8}\text{Fe}_{0.2}\text{O}_{3-\delta}$ ($0 \leq x \leq 0.2$) samples.

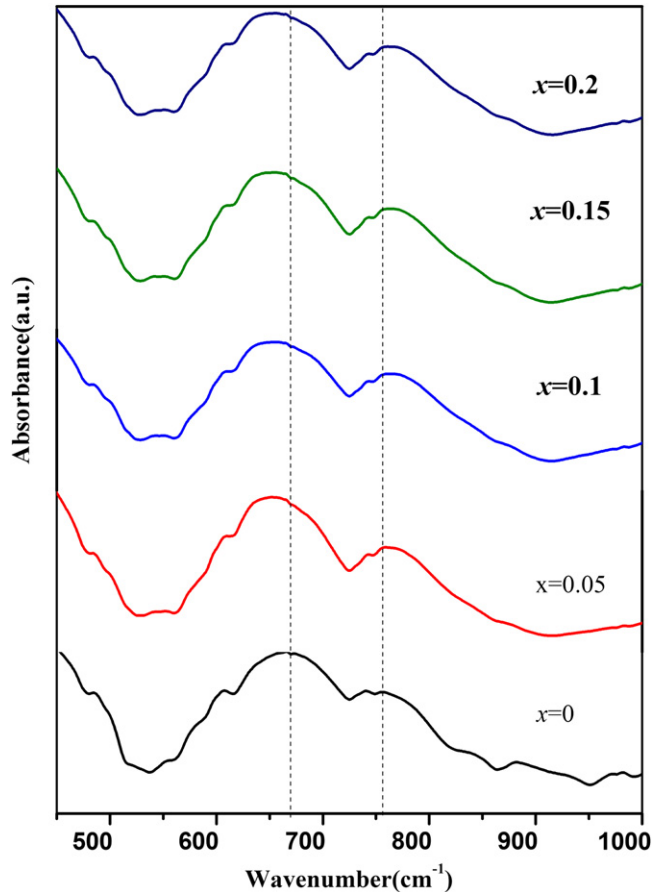


Fig. 4. Infrared spectra of the $\text{Sm}_{0.5-x}\text{Ba}_x\text{Sr}_{0.5}\text{Co}_{0.8}\text{Fe}_{0.2}\text{O}_{3-\delta}$ ($0 \leq x \leq 0.2$) samples.

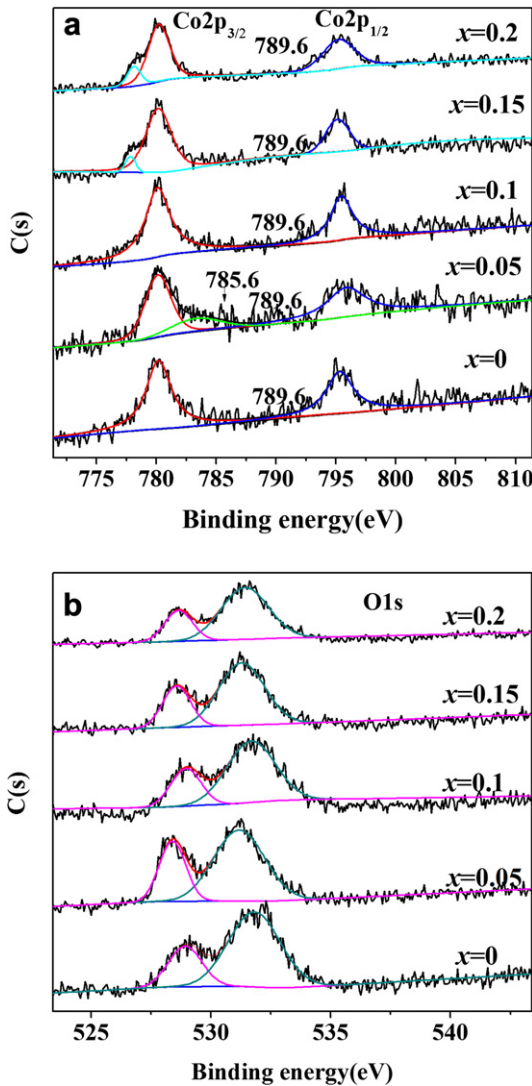


Fig. 5. (a) Co 2p and (b) O 1s XPS spectra of $\text{Sm}_{0.5-x}\text{Ba}_x\text{Sr}_{0.5}\text{Co}_{0.8}\text{Fe}_{0.2}\text{O}_{3-\delta}$ ($0 \leq x \leq 0.2$) samples.

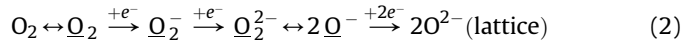
corresponding to the $\text{Co}2p_{3/2}$ and $\text{Co}2p_{1/2}$ levels. For all the SBSCF perovskite-type complex oxides, the main peak at 780.1 eV accompanied by a weak satellite shoulder at 789.6 eV indicates the existence of Co^{3+} in $\text{Sm}_{0.5-x}\text{Ba}_x\text{Sr}_{0.5}\text{Co}_{0.8}\text{Fe}_{0.2}\text{O}_{3-\delta}$, which is in agreement with the reported data for the Co peak in $\text{La}_{1-x}\text{Sr}_x\text{CoO}_3-\delta$ [36]. The low spin Co^{3+} with a binding energy of ca. 780.1 eV is attributed to octahedral Co^{3+} [37]. Shake-up satellite peaks existing near 790.0 eV is in relation with the different charge state of the spin state of Co in the perovskites. Considering the fact that the status of Co with the shake-up peak is low spin Co^{3+} in $\text{La}_{1-x}\text{Sr}_x\text{CoO}_3$ [36] and Co^{2+} in $\text{La}_{0.6}\text{Sr}_{0.4}\text{Co}_{1-y}\text{Fe}_y\text{O}_{3-\delta}$ system [8], it can be suggested that the status of the shake-up peak in SBSCF is associated with low spin Co^{3+} . For $\text{Sm}_{0.45}\text{Ba}_{0.05}\text{Sr}_{0.5}\text{Co}_{0.8}\text{Fe}_{0.2}\text{O}_{3-\delta}$ composition, the small shoulder presenting on the high binding energy side of the $\text{Co}2p_{3/2}$ spectra at ca. 785.8 eV can be identified as Co^{4+} [38]. These suggest that Co exists mainly as Co^{3+} with some Co^{4+} on the surface of the cathode materials, which is consistent with IR spectroscopy result.

The O1s XPS peaks and their deconvolution results, shown in Fig. 5b, exhibit two strong contributions, at ~ 528.3 and ~ 531.1 eV, respectively. The lower binding energy peak is well in agreement

Table 2
The composition of surface oxygen species in SBSCF oxides.

Sample	$\text{O}_{\text{lattice}}$			O_{ads}			$\text{O}_{\text{ads}}/\text{O}_{\text{lattice}}$
	Position (eV)	Area	FWHM (eV)	Position (eV)	Area	FWHM (eV)	
$x = 0$	528.8	866.5	1.72	531.7	2715.6	2.59	3.13
$x = 0.05$	528.4	1434.9	1.31	531.2	3335.9	2.44	3.00
$x = 0.10$	528.8	934.7	1.59	531.7	3037.2	2.81	3.21
$x = 0.15$	528.6	847.2	1.3	531.3	2646.1	2.35	3.28
$x = 0.2$	528.6	1223.9	1.34	531.5	4057.3	2.37	3.31

with the lattice oxygen in perovskites [39]. The higher should be attributed to the adsorbed oxygen in oxygen vacancy of this kind of defect oxides [40,8]. The relative intensity of the lower binding energy peak decreases with increasing Ba^{2+} content except for the composition with $x = 0.05$. This means an increased loss of the surface lattice oxygen with the increase of Ba^{2+} content. In the presence of oxygen, a series of transformations on the surface of oxide occurs according to the general scheme [41]:



where the underlined ions refer to chemisorbed or surface species. As showed in this scheme, different species of adsorbed oxygen are formed, gradually enriched with electrons until the state of O^{2-} is reached, which may be considered as lattice oxygen incorporated into the uppermost surface layer of the solid. When oxygen is present in the gas phase, the adsorbed oxygen species O_2^{2-} and O^- may be formed at the surface of the oxide. Moreover, these adsorbed species are strongly reactive in oxidation reactions. Therefore, the ratio of O_{ad} and $\text{O}_{\text{lattice}}$ calculated from XPS results, where O_{ad} is referred to adsorbed oxygen and $\text{O}_{\text{lattice}}$ referred to lattice oxygen, can be taken as a criterion for comparison of the oxygen reactivity. The calculated area ratio of O_{ads} and $\text{O}_{\text{lattice}}$ for $\text{Sm}_{0.5-x}\text{Ba}_x\text{Sr}_{0.5}\text{Co}_{0.8}\text{Fe}_{0.2}\text{O}_{3-\delta}$ samples is listed in Table 2. Except for $\text{Sm}_{0.45}\text{Ba}_{0.05}\text{Sr}_{0.5}\text{Co}_{0.8}\text{Fe}_{0.2}\text{O}_{3-\delta}$ sample, the area ratio of O_{ads} and $\text{O}_{\text{lattice}}$ is gradually increased with the increase of Ba^{2+} content, suggesting that the partial substitution of Ba^{2+} for Sm^{3+} will result in an improvement of the oxygen reactivity.

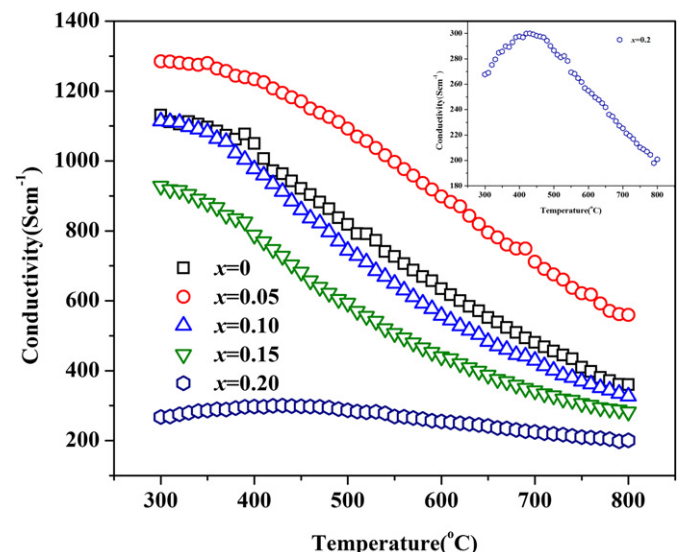
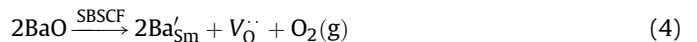
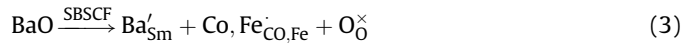


Fig. 6. The electrical conductivity (σ) of the $\text{Sm}_{0.5-x}\text{Ba}_x\text{Sr}_{0.5}\text{Co}_{0.8}\text{Fe}_{0.2}\text{O}_{3-\delta}$ ($0 \leq x \leq 0.2$) samples at the temperatures range of 300–800 $^{\circ}\text{C}$.

3.4. Electrical conductivity

The Ba^{2+} concentration dependent electrical conductivities of $\text{Sm}_{0.5-x}\text{Ba}_x\text{Sr}_{0.5}\text{Co}_{0.8}\text{Fe}_{0.2}\text{O}_{3-\delta}$ compositions are shown in Fig. 6. It is obvious that the substitution of Ba^{2+} for Sm^{3+} has a significant effect on the electrical conductivity of $\text{Sm}_{0.5-x}\text{Ba}_x\text{Sr}_{0.5}\text{Co}_{0.8}\text{Fe}_{0.2}\text{O}_{3-\delta}$. The electrical conductivity of the composition with $x=0.05$ is higher than that of the Barium-free composition. This indicates that a small amount of Ba^{2+} substituent for Sm^{3+} will result in an increase in the electrical conductivity. Whereas, the further increase of Ba^{2+} content leads to a consistent decrease in the electrical conductivity. As the cation Sm^{3+} in the A-site is replaced by the lower valency cation Ba^{2+} , according to the principle of the electron neutrality, the negative charge should be balanced either by the formation of

higher oxidation state ion at B-site or by the formation of oxygen vacancy (V_0):



According to Eq. (3), the substitution of Ba^{2+} for Sm^{3+} will lead to an enhancement of the concentration of carriers (Co, Fe $^{\cdot}$) and thereby an improvement in the electrical conductivity. This may be dominant in the case of low substitution concentration, so the electrical conductivity of the composition with $x=0.05$ is higher than that of $\text{Sm}_{0.5}\text{Sr}_{0.5}\text{Co}_{0.8}\text{Fe}_{0.2}\text{O}_{3-\delta}$. However, with the increase of

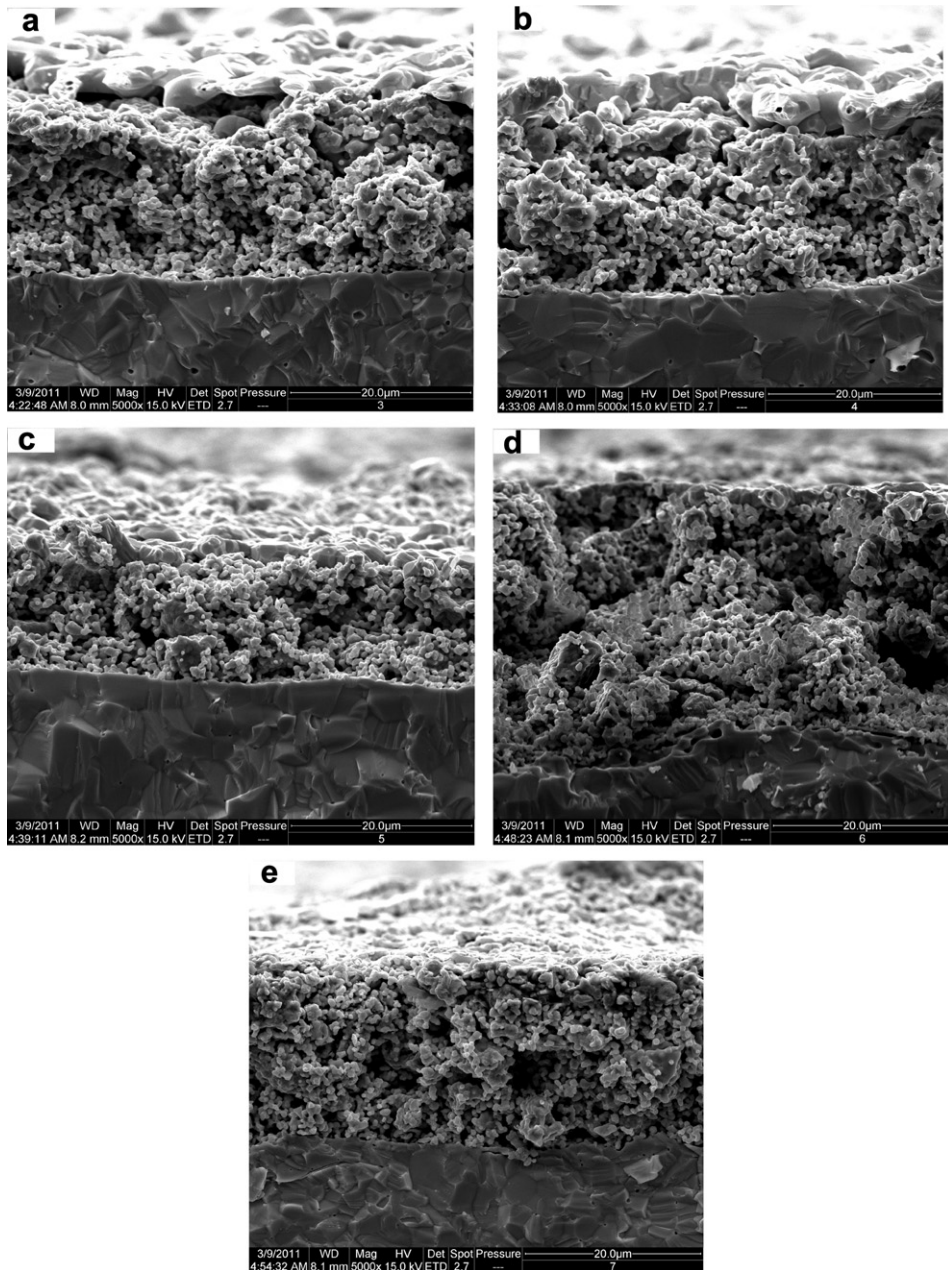


Fig. 7. Scanning electron micrographs of cutting cross section of $\text{Sm}_{0.5-x}\text{Ba}_x\text{Sr}_{0.5}\text{Co}_{0.8}\text{Fe}_{0.2}\text{O}_{3-\delta}$. (a) deposited on the SDC pellet, where the cathode is the composition (a) $x=0$, (b) $x=0.05$, (c) $x=0.10$, (d) $x=0.15$ and (e) $x=0.20$, respectively.

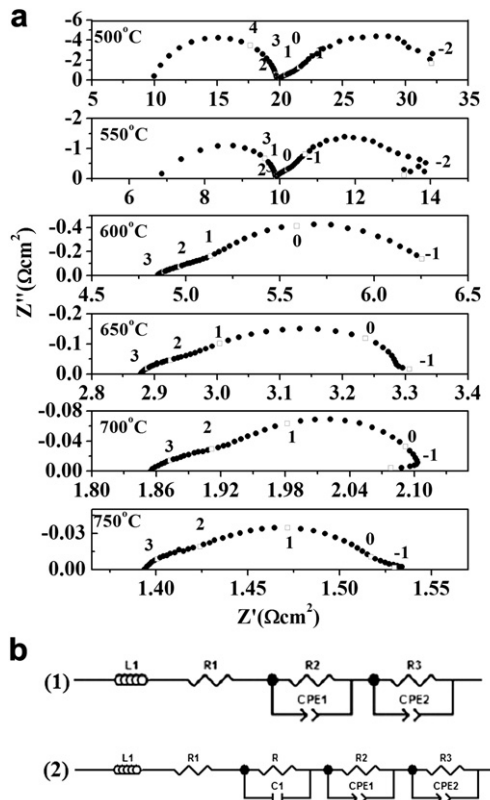


Fig. 8. (a) Impedance plots of Sm_{0.35}Ba_{0.15}Sr_{0.5}Co_{0.8}Fe_{0.2}O_{3-δ} cathode on SDC electrolyte from 500 to 750 °C and (b) equivalent circuit. The numbers in these plots correspond to logarithm of frequency.

Ba²⁺ content, the concentration of the oxygen vacancy improves. The oxygen vacancy will distort the Co–O₆ octahedron, weaken the crystal field around the Co ion and especially destroy the Co–O–Co electron transfer net, resulting in a sequential decrease in the electrical conductivity.

For the compositions with $x = 0.0$ – 0.15 , the electrical conductivities are consistently decreased with increasing temperature, which is in accordance with the metallic-like conductivity behavior. For instances, the electrical conductivity decreases from 1250 Scm⁻¹ at 300 °C to 650 Scm⁻¹ at 800 °C for the composition with $x = 0.05$. As the temperature increases, a loss reaction of oxygen from the lattice takes place, accompanied by the reduction

of Fe⁴⁺ to Fe³⁺ or Co⁴⁺ to Co³⁺, causing a decrease in the charge carriers concentration, thereby results in a decrease in the electrical conductivity. For the composition with $x = 0.2$, however, it is apparent that a semiconductor-metal transition occurs at 400–500 °C. That is, the conductivity gradually increases with the temperature, consistent with the semiconductor-like behavior, at ~450 °C it reaches the highest value, then decrease with the temperature, exhibiting a metal-like characteristics. The composition with $x = 0$ is a metallic conductor with sufficient bandwidth and little or no charge transfer gap. As Sm³⁺ ion is replaced by larger Ba²⁺ ion, the tolerance factor t decreases. This causes a bending of the (Co,Fe)–O–(Co,Fe) bonds and a decrease in the bond angle below 180°, thereby the bandwidth decrease and the charge transfer gap broaden. This might be a possible explanation of the metal to semiconductor transition for the composition with $x = 0.2$, which is in accordance with the result observed in the BSSCF system [27].

3.5. Impedance analysis

The microstructure of the Sm_{0.5}–_xBa_xSr_{0.5}Co_{0.8}Fe_{0.2}O_{3-δ} electrodes fired at 1000 °C for 5 h is examined by SEM observation. Fig. 7 shows the micrographs of the Sm_{0.5}–_xBa_xSr_{0.5}Co_{0.8}Fe_{0.2}O_{3-δ} cathodes from the cross-sectional views. It demonstrates that all the Sm_{0.5}–_xBa_xSr_{0.5}Co_{0.8}Fe_{0.2}O_{3-δ} cathodes well adhere to the electrolyte surface and are no obvious differences in the microstructure.

The complex impedance measurements of the single-phase Sm_{0.5}–_xBa_xSr_{0.5}Co_{0.8}Fe_{0.2}O_{3-δ} electrode on the SDC electrolyte were collected every 50 °C in the temperature range from 500 to 750 °C. The typical impedance spectra of Sm_{0.5}–_xBa_xSr_{0.5}Co_{0.8}Fe_{0.2}O_{3-δ} on SDC electrolyte pellet are shown in Fig. 8(a). Black circles are general impedance data points in symmetrical cells and red circles indicate decade of frequency. The impedance spectra consisted of two arcs. This indicates that there are at least two electrode processes corresponding to the two arcs during molecular oxygen reduction. The data are fitted to an equivalent circuit shown in Fig. 8(b1) and (b2). Here (RE1–CPE1) and (RE2–CPE2) represent the processes at high and low frequency, respectively. C and R represent the capacitor and resistance of the boundary of SDC electrolyte at lower temperatures. The constant phase element (CPE) represents a nonideal capacitor, and the associated CPE-Q parameter indicates the similarity of the CPE to a true capacitor, for which CPE-Q = 1. According to the impedance plots of mixed ionic and electronic conductor reported by Adler [42], charge-transfer resistant originated from ion transfer at interface of electrode and electrolyte is observed for the mid-

Table 3

The fitting results of SBSCF cathode with $x = 0.15$ on SDC electrolyte from 500 to 750 °C.

	T (°C)	500	550	600	650	700	750
L (H)	4.88×10^{-7}	5.36×10^{-7}	2.27×10^{-7}	4.45×10^{-7}	3×8810^{-7}	4.39×10^{-7}	
R_1 (Ωcm ²)	9.23	6.70	4.83	2.87	1.87		1.39
R (Ωcm ²)	10.21	2.60					
C (Fcm ⁻²)	6.77×10^{-8}	7.16×10^{-8}					
ARC ₁	R_2 (Ωcm ²)	9.15	2.49	0.90	0.28	0.11	0.11
	CPE ₁ -Q (Fcm ⁻²)	0.24	0.28	0.27	0.29	0.48	5.13×10^{-2}
	CPE ₁ -n	0.92	0.98	0.92	0.93	0.53	0.80
	C_1 (Fcm ⁻²)	0.26	0.28	0.24	0.24	2.46×10^{-2}	9.69×10^{-3}
	F_1 (Hz)	6.77×10^{-2}	0.23	0.74	2.37	88.75	662.7
ARC ₂	R_3	4.93	3.93	0.54	0.16	7.30×10^{-2}	2.48×10^{-2}
	CPE ₂ -Q (Fcm ⁻²)	0.16	0.19	0.24	0.31	0.29	0.42
	CPE ₂ -n	0.32	0.73	0.46	0.55	0.97	0.73
	C_2 (Fcm ⁻²)	9.66×10^{-2}	0.17	2.18×10^{-2}	2.65×10^{-2}	0.26	0.13
	F_2 (Hz)	0.33	0.24	13.53	37.49	5.55	10.7
	ASR (Ωcm ²)	7.96	3.97	0.81	0.25	0.10	0.08

frequency arc. For the low-frequency arc, oxygen adsorption or dissociation on the cathode surface and diffusion through the electrode bulk are likely considered to be the main contributors. To get more insight into the mechanism of oxygen reduction over the SBSCF electrode, the capacitance and angular relaxation frequency f , which is an independent parameter of sample geometric characteristics and is a very useful tool to identify the oxygen reduction process, are calculated based on the following equations [43]:

$$C_i = \frac{(R_i Q_i)^{(1/n_i)}}{R_i} \quad (5)$$

$$f_i = \frac{(R_i Q_i)^{-(1/n_i)}}{2\pi} \quad (6)$$

Table 3 summarizes the fitting parameters as a function of temperature for $\text{Sm}_{0.5-x}\text{Ba}_x\text{Sr}_{0.5}\text{Co}_{0.8}\text{Fe}_{0.2}\text{O}_{3-\delta}/\text{SDC}/\text{Sm}_{0.5-x}\text{Ba}_x\text{Sr}_{0.5}\text{Co}_{0.8}\text{Fe}_{0.2}\text{O}_{3-\delta}$ in air under zero dc bias conditions. It is observed that both frequency and capacitance for Arc1 are similar to the reported values for oxide-ion transfer through the electrolyte-electrode interface [44]. Therefore, Arc1 is assigned to the impedance associated with oxide-ion charge transfer through the interface between $\text{Sm}_{0.5-x}\text{Ba}_x\text{Sr}_{0.5}\text{Co}_{0.8}\text{Fe}_{0.2}\text{O}_{3-\delta}$ and SDC. The polarization resistance associated with this process is about 1/3–2/3 of the total cathodic resistance, suggesting that the oxygen-ion charge transfer through the electrode-electrolyte interface plays an important role in the overall oxygen reduction in the $\text{Sm}_{0.5-x}\text{Ba}_x\text{Sr}_{0.5}\text{Co}_{0.8}\text{Fe}_{0.2}\text{O}_{3-\delta}$ electrode. The angular relaxation frequency and capacitance of Arc2 is between 10^3 – 10^{-1} Hz and 10^{-2} – 10^{-3} Fcm^{-2} , respectively. Both are in the typical ranges for an electron charge transfer process [44].

Fig. 9 shows the variation of the impedance spectra of the $\text{Sm}_{0.5-x}\text{Ba}_x\text{Sr}_{0.5}\text{Co}_{0.8}\text{Fe}_{0.2}\text{O}_{3-\delta}$ cathodes with Ba content increasing at 700 °C. **Table 4** summarizes the fitting parameters as a function of Ba^{2+} content for the $\text{Sm}_{0.5-x}\text{Ba}_x\text{Sr}_{0.5}\text{Co}_{0.8}\text{Fe}_{0.2}\text{O}_{3-\delta}/\text{SDC}/\text{Sm}_{0.5-x}\text{Ba}_x\text{Sr}_{0.5}\text{Co}_{0.8}\text{Fe}_{0.2}\text{O}_{3-\delta}$ symmetry cells tested in air under zero dc bias condition. It is obvious that the intercept of the impedance arc on the real axis decreases with increasing Ba^{2+} concentration, which indicates that the partial substitution of Ba^{2+} for Sm^{3+} results in a significant decrease in the interfacial polarization resistance R_p . For instance, the interfacial polarization resistance for the composition with $x=0.20$ is 0.097 Ωcm^2 at 700 °C, which is less than half of that for the composition $\text{Sm}_{0.5}\text{Sr}_{0.5}\text{Co}_{0.8}\text{Fe}_{0.2}\text{O}_{3-\delta}$. As mentioned above, when Sm^{3+} is partially substituted by Ba^{2+} , the cell of the perovskite expands, oxygen vacancy concentration increases and the oxygen reactivity improves. The decrease in the polarization resistance is the result of the above factors.

The Area Specific Resistance can be calculated using the following equation:

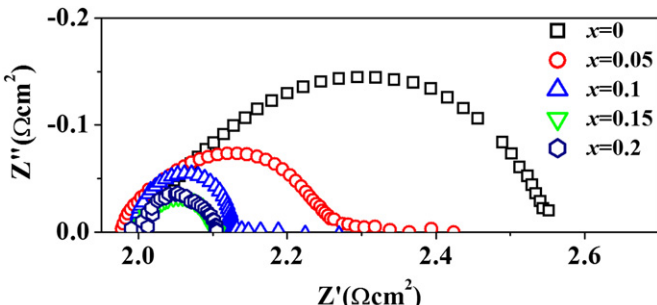


Fig. 9. Impedance spectra of $\text{Sm}_{0.5-x}\text{Ba}_x\text{Sr}_{0.5}\text{Co}_{0.8}\text{Fe}_{0.2}\text{O}_{3-\delta}$ ($0 \leq x \leq 0.2$) at 700 °C.

Table 4
The fitting results of SBSCF cathodes for various Ba content at 700 °C.

Sample	$x = 0$	$x = 0.05$	$x = 0.1$	$x = 0.15$	$x = 0.2$
L (H)	5.58×10^{-7}	6.13×10^{-7}	6.23×10^{-7}	3×8810^{-7}	5.85×10^{-7}
R_1 (Ωcm^2)	1.85	1.81	1.92	1.87	1.89
ARC ₁ R_2 (Ωcm^2)	0.19	0.16	0.13	0.11	0.11
CPE _{1-Q} (Fcm^{-2})	0.14	3.81×10^{-2}	0.49	0.48	9.32×10^{-2}
CPE _{1-n}	0.50	0.73	0.77	0.53	0.70
C_1 (Fcm^{-2})	3.72×10^{-3}	5.78×10^{-3}	0.22	2.46×10^{-2}	1.31×10^{-2}
F_1 (Hz)	225.0	172.3	5.69	88.75	110.6
ARC ₂ R_3	0.36	0.22	0.25	7.30×10^{-2}	6.54×10^{-2}
CPE _{2-Q} (Fcm^{-2})	0.19	9.45×10^{-2}	4.91×10^{-2}	0.29	2.52×10^{-2}
CPE _{2-n}	0.75	0.30	0.50	0.97	0.98
C_2 (Fcm^{-2})	7.77×10^{-2}	1.80×10^{-2}	6.03×10^{-4}	0.26	2.21×10^{-2}
F_2 (Hz)	5.7	40.3	1056.8	5.55	110.1
ASR (Ωcm^2)	0.31	0.21	0.21	0.10	9.76×10^{-2}

$$\text{ASR} = R_p \cdot S/2 \quad (7)$$

where S is the cathode surface, R_p is the difference between the two intercepts at high and low frequencies in the real axis, and the coefficient 2 of the denominator accounts for the fact that the cell is symmetrical. The Arrhenius plots of the Area Specific Resistance for $\text{Sm}_{0.5-x}\text{Ba}_x\text{Sr}_{0.5}\text{Co}_{0.8}\text{Fe}_{0.2}\text{O}_{3-\delta}$ cathodes are shown in **Fig. 10**. The Area Specific Resistance is consistently decreased with the increase of Ba^{2+} content, namely it decreases from 0.31 Ωcm^2 for $\text{Sm}_{0.5}\text{Sr}_{0.5}\text{Co}_{0.8}\text{Fe}_{0.2}\text{O}_{3-\delta}$ cathode to 0.09 Ωcm^2 for the composition with $x=0.2$ at 700 °C, from 2.61 Ωcm^2 to 1.32 Ωcm^2 at 600 °C. In addition, for these $\text{Sm}_{0.5-x}\text{Ba}_x\text{Sr}_{0.5}\text{Co}_{0.8}\text{Fe}_{0.2}\text{O}_{3-\delta}$ cathodes, the activation energy is in the range of 1.23 ~ 1.46 eV.

Oxygen reduction at a porous cathode includes a sequence of steps: (i) adsorption of oxygen from the gas phase to the surface of the porous cathode, (ii) dissociation of adsorbed oxygen molecule into atomic oxygen at the active sites, (iii) surface diffusion of oxygen atom, (iv) charge transfer; and (v) diffusion of O^{2-} ions through the cathode across the cathode/electrolyte interface and into the electrolyte. Cathode polarization resistance is closely

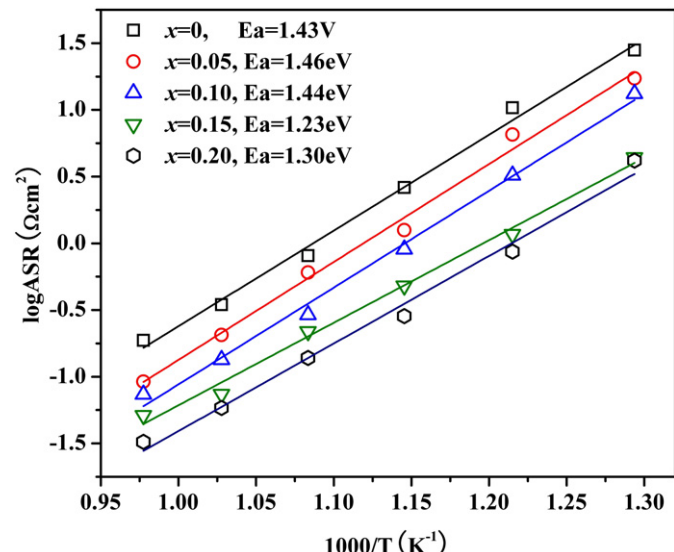


Fig. 10. Area specific resistance (ASR) results of $\text{Sm}_{0.5-x}\text{Ba}_x\text{Sr}_{0.5}\text{Co}_{0.8}\text{Fe}_{0.2}\text{O}_{3-\delta}$ ($0 \leq x \leq 0.2$) with respect to the temperature.

related not only to the charge transfer and the adsorption/dissociation of oxygen, but also to the transport speed of oxide ions through the cathode bulk and across the cathode/electrolyte interface. Therefore, the kinetics of the oxygen exchange and the diffusion of oxide ions in the cathode as well as the electronic conductivity play a critical role on the oxygen reduction reaction.

Compared to the Barium-free composition, the reaction activity enhancement for Ba-containing compositions should be mainly due to the following two reasons. The first one is the increase in the content of oxygen vacancies in $\text{Sm}_{0.5-x}\text{Ba}_x\text{Sr}_{0.5}\text{Co}_{0.8}\text{Fe}_{0.2}\text{O}_{3-\delta}$. Generally, the adsorption of O_2 by perovskites oxides is related to the surface area and oxygen vacancies. The content of surface adsorbed oxygen and oxygen vacancy concentration of $\text{Sm}_{0.5-x}\text{Ba}_x\text{Sr}_{0.5}\text{Co}_{0.8}\text{Fe}_{0.2}\text{O}_{3-\delta}$ increase with the increase of Ba^{2+} concentration, which is indicated by XPS analysis. The presence of a large amount of oxygen vacancies would accelerate the mobility of lattice oxygen and facilitate to the reproduction of oxygen vacancies, which increases the adsorption and activation of oxygen reduction reaction. The second one is that the structural

modifications induced by Ba^{2+} also contributes to increase the distance between the two cationic positions and to weaken the tilting of the oxygen octahedra around the B cations, which will benefit the transport of the mobile oxygen ion.

3.6. Single-cell performance of anode-supported solid oxide fuel cell with $\text{Sm}_{0.5-x}\text{Ba}_x\text{Sr}_{0.5}\text{Co}_{0.8}\text{Fe}_{0.2}\text{O}_{3-\delta}$

Fig. 11 shows the power density and voltage as a function of current density for Ni–SDC/SDC/ $\text{Sm}_{0.5-x}\text{Ba}_x\text{Sr}_{0.5}\text{Co}_{0.8}\text{Fe}_{0.2}\text{O}_{3-\delta}$ cells using H_2 as the fuel and static air as the oxidant in the temperature range 500–650 °C, respectively. The open-circuit voltage (OCV) is lower than 1.0 V, and decreases with the increase of the temperature. The decrease in OCV should be attributed to the internal current in the SDC electrolyte film caused by the reduction of some Ce^{4+} to Ce^{3+} . The power density increases with increasing Ba^{2+} content and reach the maximum values for the cells using $\text{Sm}_{0.3}\text{Ba}_{0.2}\text{Sr}_{0.5}\text{Co}_{0.8}\text{Fe}_{0.2}\text{O}_{3-\delta}$ as cathode material. The maximum power densities for the $\text{Sm}_{0.3}\text{Ba}_{0.2}\text{Sr}_{0.5}\text{Co}_{0.8}\text{Fe}_{0.2}\text{O}_{3-\delta}$ based cells are

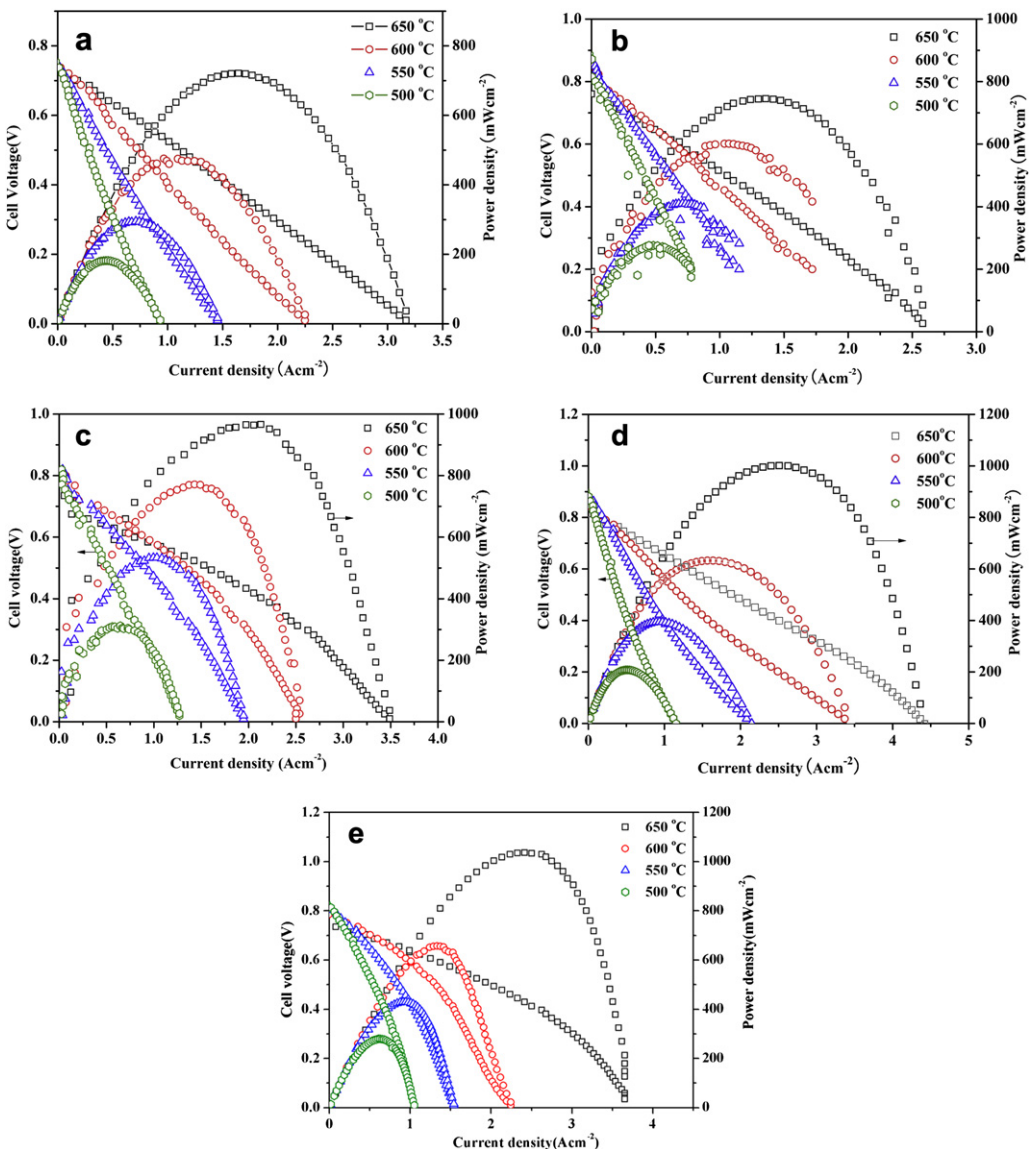


Fig. 11. Cell voltage (left axis) and power density (right axis) as a function of the current density for the test cell with the configuration SDC + Ni/SDC/ $\text{Sm}_{0.5-x}\text{Ba}_x\text{Sr}_{0.5}\text{Co}_{0.8}\text{Fe}_{0.2}\text{O}_{3-\delta}$, where the cathode is the composition (a) $x = 0$, (b) $x = 0.05$, (c) $x = 0.10$, (d) $x = 0.15$ and (e) $x = 0.20$, respectively.

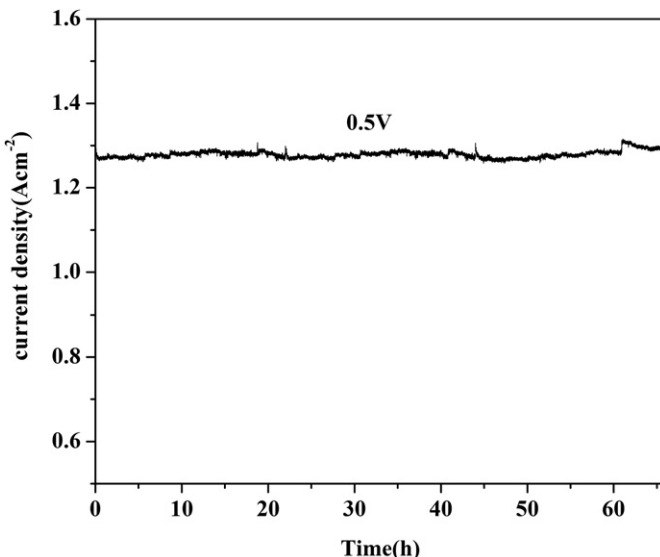


Fig. 12. Short-term stability of the cells tested at a constant cell voltage of 0.5 V at 600 °C.

285 mWcm⁻² at 500 °C, 423 mWcm⁻² at 550 °C, 656 mWcm⁻² at 600 °C and 1030 mWcm⁻² at 650 °C. These values are much higher than those exhibited by the $\text{Sm}_{0.5}\text{Sr}_{0.5}\text{Co}_{0.8}\text{Fe}_{0.2}\text{O}_{3-\delta}$ cathodes, which are 182, 292, 468 and 720 mWcm⁻² at 500 °C, 550 °C, 600 °C, 650 °C, respectively. Since the anodes and electrolyte are fabricated following an identical procedure, the anode and electrolyte resistances of various cells are reasonably assumed to be the same. Consequently, the main contribution to the enhancement in the cell performance is from the substitution of Ba²⁺ for Sm³⁺ of SBSCF cathode. As mentioned above, the substitution results in a decrease in the electrical conductivity and an increase in the oxygen reactivity. Hence, the improved electrochemical performance with increasing of Ba²⁺ content should be mainly ascribed to the enhanced oxygen reactivity, which includes the improvement in the oxygen bulk diffusion rate as well as in the surface exchange kinetics. It provides a promising approach to development of high performance cathodes for IT-SOFCs.

The short-term stability of Ni-SDC/SDC/SBSCF ($x = 0.20$) cell was also investigated. The cell was ran for a few days with a constant voltage loading of 0.5 V and a constant operating temperature condition of 600 °C, the corresponding cell current response was recorded. As it can be seen from Fig. 12 that the cell current response is almost constant, no detectable degradation is observed, implying SBSCF cathode has high electrochemical performance stability. However, the long-term stability needs a further depth testing.

4. Conclusions

In this work, $\text{Sm}_{0.5-x}\text{Ba}_x\text{Sr}_{0.5}\text{Co}_{0.8}\text{Fe}_{0.2}\text{O}_{3-\delta}$ (SBSCF) perovskite with an orthorhombic structure is prepared by a citric acid method. The effects of Ba²⁺ substituent for Sm³⁺ on the structure and electrochemical properties of $\text{Sm}_{0.5-x}\text{Ba}_x\text{Sr}_{0.5}\text{Co}_{0.8}\text{Fe}_{0.2}\text{O}_{3-\delta}$ (SBSCF) are investigated. The XRD, Raman, IR, and XPS results indicate that the structure continuously varies with the Ba²⁺ content. As a result, $\text{Sm}_{0.5-x}\text{Ba}_x\text{Sr}_{0.5}\text{Co}_{0.8}\text{Fe}_{0.2}\text{O}_{3-\delta}$ based cells exhibit a regular variation in the electrical conductivity, area specific resistance and power density with Ba²⁺ content. That is, the electrical conductivity decreases with Ba²⁺ content, while the area specific resistance and power density improve with Ba²⁺ content. $\text{Sm}_{0.3}\text{Ba}_{0.2}\text{Sr}_{0.5}\text{Co}_{0.8}\text{Fe}_{0.2}\text{O}_{3-\delta}$ cathode shows the best electrochemical

performance. The ASRs are 0.056 Ωcm² at 700, 0.032 Ωcm² at 750 °C, respectively, and the power densities are 1030 mWcm⁻² at 650 °C, 280 mWcm⁻² at 500 °C. These results suggest that the substitution of Ba²⁺ for Sm³⁺ results in significant enhancement in the electrochemical performance of SBSCF at 500–700 °C. This provides an approach to the improvement of the electrochemical properties for the current cathodes through changing the structure by doping Ba²⁺.

Acknowledgements

This work was supported by the Program for New Century Excellent Talents in University, National Natural Science Foundation of China under contract Nos.50872049 and Natural Science Foundation of Inner Mongolia autonomous region 2010Zd04.

References

- [1] B.C.H. Steele, A. Heinzel, *Nature* 414 (2001) 345–352.
- [2] T. Ishihara, S. Fukui, H. Nishiguchi, Y. Takita, *Solid State Ionics* 609 (2002) 152–153.
- [3] N.P. Brandon, S. Skinner, B.C.H. Steele, *Annu. Rev. Mater. Res.* 33 (2003) 183–213.
- [4] F. Bidrawn, S. Lee, J.M. Vohs, R.J. Gorte, *J. Electrochem. Soc.* 155 (2008) B660–B665.
- [5] A. Manthiram, F. Prado, T. Armstrong, *Solid State Ionics* 152 (2002) 647–655.
- [6] V.V. Kharton, A.A. Yaremchenko, A.A. Valente, V.A. Sobyanin, V.D. Belyaev, G.L. Semin, S.A. Veniaminov, E.V. Tsipis, A.L. Shaula, J. Frade, R. Rocha, *Solid State Ionics* 176 (2005) 781–791.
- [7] J. Caro, H.H. Wang, C. Tablet, A. Kleinert, A. Feldhoff, T. Schiestel, M. Kilgus, P. Kolsch, S. Werth, *Catal. Today* 118 (2006) 128–135.
- [8] M.M. Natile, F. Poletto, A. Galenda, A. Glisenti, T. Montini, L.D. Rogatis, P. Fornasiero, *Chem. Mater.* 20 (2008) 2314–2327.
- [9] R. Chiba, F. Yoshimura, Y. Sakurai, *Solid State Ionics* 124 (1999) 281–288.
- [10] S.C. Singhal, *Solid State Ionics* 135 (2000) 305–313.
- [11] W.G. Wang, M. Mogensen, *Solid State Ionics* 176 (2005) 457–462.
- [12] A. Yamada, K. Saka, M. Uehara, S. Taminato, R. Kanno, F. Mauvy, C. Grenier, *Electrochem. Commun.* 12 (2010) 1690–1693.
- [13] H.E. Shinawi, C. Greaves, *J. Solid State Chem* 181 (2008) 2705–2712.
- [14] Q. Li, Y. Fan, H. Zhao, L.P. Sun, L.H. Huo, *J. Power Sources* 167 (2007) 64–68.
- [15] Y.N. Kim, J.H. Kim, A. Manthiram, *J. Power Sources* 195 (2010) 6411–6419.
- [16] S.M. Haile, *Acta Mater.* 51 (2003) 5981–6000.
- [17] J.H. Kim, Y. Kim, P.A. Connor, J.T.S. Irvine, J. Bae, W. Zhou, *J. Power Sources* 194 (2009) 704–711.
- [18] D. Chen, R. Ran, K. Zhang, J. Wang, Z. Shao, *J. Power Sources* 188 (2009) 96–105.
- [19] J.H. Kim, M. Cassidy, T.S. John, J. IrvineBae, *J. Mater. Chem.* 22 (2010) 883–892.
- [20] C.R. Xia, W. Rauch, F.L. Chen, M.L. Liu, *Solid State Ionics* 149 (2002) 11–19.
- [21] M. Sahibzada, B.C.H. Steele, K. Zheng, R.A. Rudkin, J.M. Bae, N. Kiratzis, I.S. Metcalfe, in: *Proc. 2nd European Solid Oxide Fuel Cell Forum*, Oslo (1996), p. 687.
- [22] E.P. Murray, M.J. Sever, S.A. Barnett, *Solid State Ionics* 148 (2002) 27–34.
- [23] S.W. Baek, J. Bae, Y.S. Yoo, *J. Power Sources* 193 (2009) 431–440.
- [24] G. Zhang, X. Dong, Z. Liu, W. Zhou, Z.P. Shao, W. Jin, *J. Power Sources* 195 (2010) 3386–3393.
- [25] H. Lv, Y. Wu, B. Huang, B. Zhao, K. Hu, *Solid State Ionics* 177 (2006) 901–906.
- [26] Z.P. Shao, S.M. Haile, *Nature* 431 (2004) 170–173.
- [27] S. Li, Z. Lü, X. Huang, B. Wei, W. Su, *Solid State Ionics* 178 (2007) 417.
- [28] S. Li, Z. Lü, X. Huang, W. Su, *Solid State Ionics* 178 (2008) 1853.
- [29] S. Li, Z. Lü, X. Huang, B. Wei, W. Su, *J. Phys. Chem. Solid* 68 (2007) 1707.
- [30] J. Richter, P. Holtappels, T. Graul, T. Nakamura, L.J. Gauckler, *Monatsh. Chem.* 140 (2009) 985–999.
- [31] H. Hayashi, H. Inaba, M. Matsuyama, N.G. Lan, M.D. Okiya, H. Tagawa, *Solid State Ionics* 122 (1999) 1–15.
- [32] R.D. Shannon, *Acta Cryst. A32* (1976) 751–767.
- [33] V.B. Podobedov, A. Webet, D.B. Romero, J.P. Rice, H.D. Drew, *Solid State Commun.* 105 (1998) 589–593.
- [34] K. Li, X. Li, K. Zhu, J. Zha, Y. Zhang, *J. Appl. Phys.* 81 (1997) 6943–6946.
- [35] N.A. Merino, B.P. Barbero, P. Grange, L.U. Cadús, *J. Catal.* 231 (2005) 232–244.
- [36] K. Tabata, I. Matsumoto, S. Kohiki, *J. Mater. Sci.* 22 (1987) 1882–1886.
- [37] G.H. Li, L.Z. Dai, D.S. Lu, S.Y. Peng, *J. Solid State Chem.* 89 (1990) 167–173.
- [38] P. Wang, L. Yao, M. Wang, W. Wu, *J. Alloys Comp.* 311 (2000) 53–56.
- [39] Y.G. Wang, J.W. Ren, Y.Q. Wang, F.Y. Zhang, X.H. Liu, Y. Guo, G.Z. Lu, *J. Phys. Chem. C* 112 (2008) 15293–15298.
- [40] R.Q. Tan, Y.F. Zhu, *Appl. Catal. B Environ.* 58 (2005) 61–68.
- [41] N.A. Merino, B.P. Barbero, P. Eloy, L.E. Cadús, *Appl. Surf. Sci.* 253 (2006) 1489–1493.
- [42] S.B. Adler, *Solid State Ionics* 135 (2000) 603–612.
- [43] M.J. Escudero, A. Aguadero, J.A. Alonso, L. Daza, *J. Electroanal. Chem.* 611 (2007) 107–116.
- [44] S.B. Adler, X.Y. Chen, J.R. Wilson, *J. Catal.* 245 (2007) 91–109.